Manuscript

Measurement report: Crustal materials play an increasing role in elevating particle pH: Insights from 12-year records in a typical inland city of China.

Hongyu Zhang[1, 2], Shenbo Wang [2, 3]*, Zhangsen Dong [1, 2]*, Xiao Li [2, 3], Ruiqin Zhang[2, 3]

[1] Collage of Chemistry, Zhengzhou University, Zhengzhou, 450000, China

[2] Research Institute of Environmental Sciences, Zhengzhou University, Zhengzhou 450000, China

[3] School of Ecology and Environment, Zhengzhou University, Zhengzhou, 450000, China

* Corresponding authors: Shenbo Wang and Zhangsen Dong

E-mail address: shbwang@zzu.edu.cn and dzszzu1990@163.com

Abstract

Particle acidity serves as a key determinant in atmospheric chemical processes. Emerging concerns regarding aerosol acidity trends have been highlighted amid China's sustained initiatives to mitigate emissions of both acidic and alkaline precursors, especially in North China, which is significantly affected by dust aerosol. 12-year observational data in Zhengzhou reveal that the annual average $PM_{2.5}$ concentration decreased from 162 ± 81 μg/m^3 in 2011 to 60 ± 41 μg/m^3 in 2022, with the largest reduction in sulfate (73%). Correspondingly, the annual particle pH increased by 0.10 units from 2011 to 2019. In addition, the elevated particle pH in 2015 and 2018 was notably influenced by the increase in TNH_x (NH_3 + NH_4^+). Note that the crustal material concentrations and their proportions increased significantly during 2019–2022, which might be responsible for the resuspension of surrounding soil dust. Even though the TNH_x concentration was decreasing, the annual average growth rate of pH values increased to 0.21 units from 2019 to 2022. This phenomenon is not unique to Zhengzhou, as major cities in the North China Plain have also experienced a pronounced upward trend in coarse particles after 2019. Therefore, the long-term evolution of particle acidity in North China will require comprehensive consideration of synergistic effects involving acidic precursors, ammonia, and crustal materials.

Keywords: Dust, aerosol acidity, sources, North China Plain, control measurement

Synopsis: The future ammonia reduction policies in North China may not lead to a rapid increase in particle acidity in the presence of crustal materials., which further elevated the particle pH after 2019.

Graphical abstract:

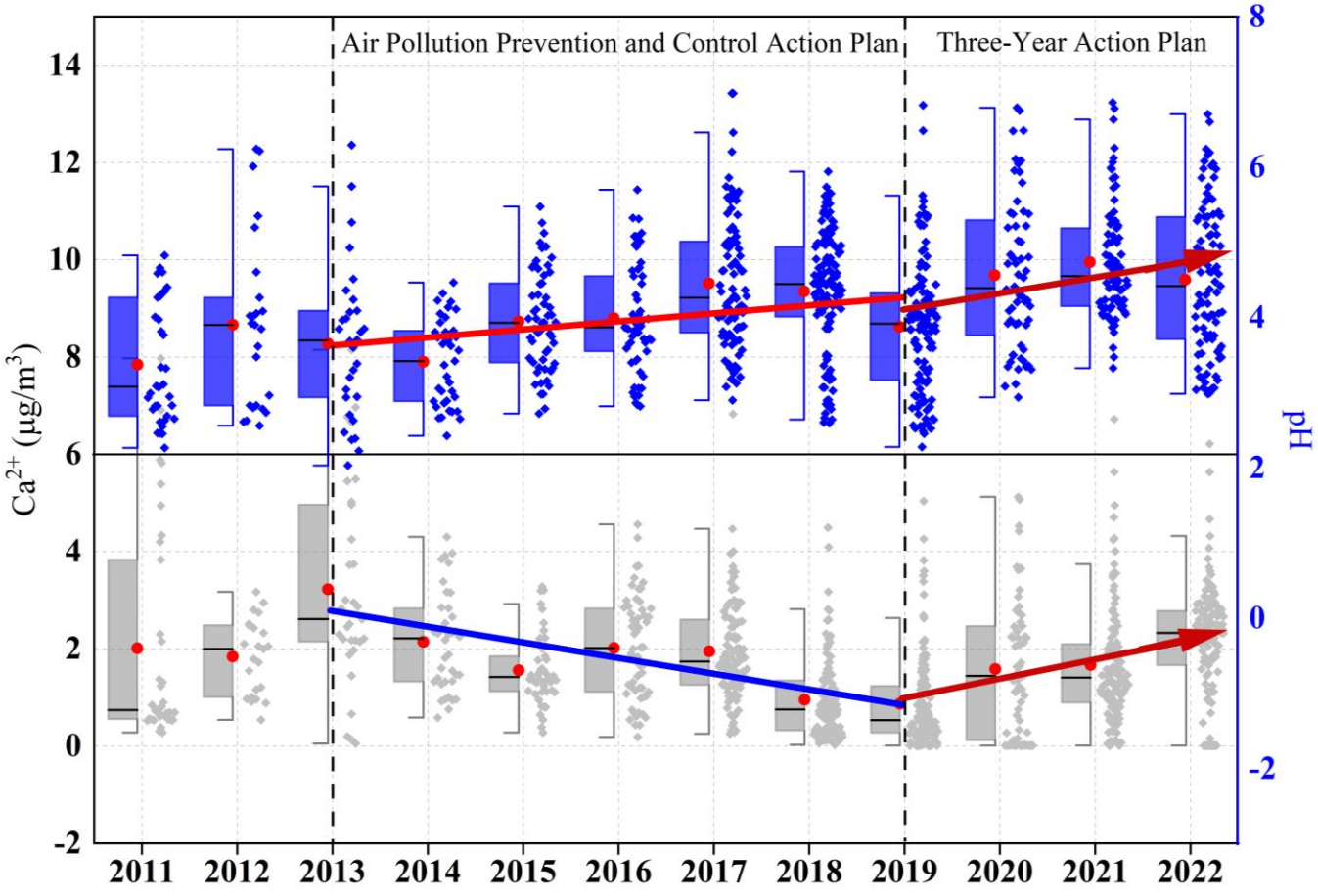

Highlights:

- Crustal material concentrations and their proportions increased significantly during 2019–2022;
- The resuspension of surrounding soil dust may determine the rebound of crustal material concentrations;
- Rebound in crustal material further elevated the particle pH.

1 Introduction

Particle acidity is a critical parameter that affects atmospheric chemistry, such as the gas-particle partitioning of semi-volatile and volatile species (Surratt et al., 2010; Guo et al., 2016), the solubility of metals (Tao and Murphy, 2019), acid-catalyzed reactions (Rengarajan et al., 2011), and acid deposition (Mao et al., 2009), thereby determining aerosol concentration and chemical composition, as well as impacting human health, ecosystems, and climate (Li et al., 2017; Pye et al., 2020; Su et al., 2020; Nenes et al., 2021). Generally, the global fine particulate matter ($PM_{2.5}$, aerodynamic diameter ≤ 2.5 μm) exhibits a bimodal pH distribution ranging from 1–3 (e.g., in the United States and Europe) (Guo et al., 2015; Battaglia et al., 2017; Masiol et al., 2020; Zhang et al., 2021) and 4–5 (e.g., in East Asia) (Kim et al., 2022; Sharma et al., 2022). The atmosphere rich in gaseous ammonia (NH_3) and crustal material (CM) shows significant pH buffering effects (Wang et al., 2020; Zheng et al., 2020; Karydis et al., 2021), which is a dominant factor that drives the high particle pH in East Asia (Karydis et al., 2021; Zhang et al., 2021; Kim et al., 2022; Sharma et al., 2022).

In recent years, the changing trends in particle pH have become a research focus, especially in China, in response to air pollution control policies, i.e. Air Pollution Prevention and Control Action Plan (2013–2018) and Three-Year Action Plan (2018–2020). The annual average $PM_{2.5}$ concentration in Beijing dropped by 64% from 89.5 μg/m³ in 2013 to 32 μg/m³ in 2023 (MEP, 2023), with a clear downward trend of sulfate concentration, and nitrate surpassing sulfate as the primary component (Zhai et al., 2019; Zhou et al., 2019; Li et al., 2023). The atmospheric behavior of ammonium, governed by gas-particle partitioning processes involving ammonia (NH_3) as the predominant alkaline gas,

demonstrates notable stability in concentration levels, with observational records showing less than 5% interannual variation in NH_3 column densities over North China during 2015–2019 (Dong et al., 2023). Under such conditions, the dominant inorganic aerosol component transitions from ammonium sulfate to ammonium nitrate. This compositional shift enhances atmospheric particulate hygroscopicity due to ammonium nitrate's superior water uptake capability, ultimately elevating particle pH levels through aqueous-phase dilution mechanisms (Wexler and Seinfeld, 1991; Pinder et al., 2007, 2008; Heald et al., 2012; Weber et al., 2016). For instance, a significant increase in the nitrate-to-sulfate molar ratio from 2014–2017 in Beijing resulted in the particle pH increasing from 4.4 to 5.4 (Xie et al., 2020). Moreover, increased NH_3 concentrations raised particle pH by 0.3–0.4 units from 2014/2015 to 2018/2019 in Beijing (Song et al., 2019). Over Europe and North America, the pH has increased strongly from about 2.8 and 2.2 during the 1970s to 3.9 and 3.3 in 2020 respectively, especially during the 1990s, with significantly increasing NH_3 emission (Karydis et al., 2021). On the contrary, modeling results indicate a continuous decline in pH in East Asia from 1970 to 2020 due to sharp increases in SO_2 and NO_x emissions (Karydis et al., 2021). In addition, the $PM_{2.5}$ pH showed a slight decrease of 0.13 from 2018 to 2022 summer in Beijing due to the change in total nitrate ($NO_3^- + HNO_3$) (Li et al., 2023). Moreover, Zhou et al. (2022) found a decreasing pH trend from 2011 to 2019 in eastern China, primarily influenced by temperature, followed by sulfate and non-volatile cations. Similarly, Nah et al. (2023) observed a decreasing pH trend from 2011 to 2020 in Hong Kong, attributing it to temperature and sulfate levels. Thus, concerns have been raised about the potential increase in the acidity of aerosol and precipitation due to China's ongoing efforts to reduce ammonia emissions, which pose severe health risks and acid deposition (Liu et al., 2019; Shi al., 2019).

In addition to NH_3, CM is another key alkaline substance, that buffers particle pH. Ca^{2+} can form insoluble $CaSO_4$ with sulfate, reducing sulfate concentration in the aqueous phase of aerosol, and thus lowering H^+ and aerosol liquid water content (ALWC) concentrations and enhancing particle pH (Ding et al., 2019; Karydis et al., 2021). Moreover, non-volatile cations can lower the molar ratio of ammonia to sulfate, leading to an increase in particle pH (Zheng et al., 2022). Karydis et al. (2021) framework demonstrated that CM played a critical buffering role in sustaining aerosol pH around 7 across the Middle East arid regions. The model sensitivity tests revealed that under hypothetical dust-free conditions (CM = 0), aerosol acidity would escalate to pH~4 due to NH_4^+/SO_4^{2-} domination. Wang et al. (2022) reported that non-volatile cations accounted for approximately 8–17% of hourly aerosol pH variation. Li et al. (2023) indicated that the buffering effect of cations was the major reason for the relatively small pH changes from 2018 to 2022 in Beijing, emphasizing that reducing coarse particle emissions in the future could significantly decrease particle pH. In addition, there was a rising trend in the contribution of CM to particle pH in Tianjin, China (Shi et al., 2017). Therefore, it is evident that CM has a significant impact on the variation of particle pH, especially in North China, which is significantly affected by dust aerosol, but the trend of CM concentration and its long-term implication is still lacking unfortunately.

Zhengzhou presents unique atmospheric chemistry that distinguishes it from other mega-cities in North China. As the capital of China's foremost agricultural province (Henan Province, contributing 18% of national NH_3 emissions), Zhengzhou's $PM_{2.5}$ composition combined substantial crustal material (15 ± 3% in $PM_{2.5}$ vs. <10% in Beijing) with exceptional ammonia abundance (Huang et al., 2012; Liu et al., 2018; Wang et al., 2018). This created distinct particle acidity characteristics,

maintaining pH 4.5–6.0 compared to lower pH levels (3.3–5.4) in other cities like Beijing (Ding et al.,2019; Zhang et al., 2021). However, two critical research gaps persist: (1) the long-term evolution of CM under control policies remains unquantified; (2) the role of CM on pH buffer capacity in NH_3-enriched environments lacks systematic assessment.

To address these gaps, our study pioneers the first multi-decadal analysis (2011–2022) coupling $PM_{2.5}$ components with thermodynamic modeling through three key innovations: (1) revealing the long-term trends of CM, (2) analyzing the variations of CM sources, and (3) exploring pH trend and its relationship with CM. The resultant findings advance our understanding of urban aerosol acidity chemistry by underscoring the critical role of CM.

2 Experiment and method

2.1 Instruments and Measurements

Sampling was conducted on the fourth-floor platform at Zhengzhou University (34.75° N, 113.61° E) in Zhengzhou, China. The sampling site (Fig. S1), approximately 14 m above the ground, is primarily surrounded by residential areas with well-developed transportation networks and no significant industrial sources. There are two highways located 3 km to the south and 7 km to the east. Additionally, a coal-fired power plant located 6 km to the east was shut down in 2020, and a gas-fired power plant is situated 3 km to the south.

Samples were collected using a high-volume sampler (TE-6070D, Tisch, USA) and air particulate samplers (TH-16A, Tianhong, China) from April 2011 to December 2022. Two quartz filters and two

Teflon filters were used daily from 10:00 AM to 9:00 AM the next day, resulting in a total of 5848 samples. After excluding abnormal data due to instrument malfunctions, 4228 valid samples were obtained. Detailed information on the samples is provided in Table S1. Organic carbon (OC) and elemental carbon (EC) were analyzed using a carbon analyzer (Model 5L, Sunset Laboratory, USA). Water-soluble inorganic ions (Cl^-, NO_3^-, SO_4^{2-}, Na^+, NH_4^+, K^+, Mg^{2+}, and Ca^{2+}) were measured using ion chromatography (ICS-90 and ICS-900 models, Dionex, USA) (Yu et al., 2017; Jiang et al., 2018). Elements were analyzed using a wavelength dispersive X-ray fluorescence spectrometer (S8 TIGER, Bruker, Germany) to determine concentrations of Fe, Na, Mg, Al, Si, Cl, K, Ca, V, Ni, Cu, Zn, Cr, Mn, Co, Cd, Ga, As, Se, Sr, Sn, Sb, Ba, and Pb (Tremper et al., 2018). Meteorological conditions, including temperature (T), relative humidity (RH), and wind speed (WS) were obtained using an automatic weather station (Wang et al., 2019). Blank filters were also routinely analyzed with each batch of samples to detect sample contamination and provide quality assurance on the elemental concentrations. Detailed analytical methods and quality control are described in the supplement (Text S1). The method detection limits and measurement uncertainties are summarized in Table S2. The quality assurance protocol excluded temporally discrete dust storm and precipitation periods to prevent contamination of the source analysis of CM and modeling particle pH, given that such events induce non-representative extremes in both crustal element concentrations and pH values, coupled with elevated PM measurement uncertainties. The annual mean $PM_{2.5}$ concentration data for cities in the North China Plain were obtained from the China National Environmental Monitoring Center (CNEMC), available at https://www.cnemc.cn/.

2.2 Data Analysis

2.2.1 Mass reconstruction

The calculation method for CM is as follows (Tian et al., 2016):

$$[CM]=1.89\times[Al] + 2.14\times[Si] + 1.4\times[Ca] + 1.43\times[Fe]+1.94[Ti] \quad (1)$$

where [Al], [Si], [Ca], [Fe] and [Ti] represent the concentrations of the respective elements (μg/m^3), but Ti was not measured.

2.2.2 Thermodynamic model

The particle pH was calculated using the ISORROPIA-II mode (version 2.1, http://isorropia.eas.gatech.edu). The input data (excluding RH ≤ 30%), including SO_4^{2-}, TNO_3 (HNO_3 + NO_3^-), TNH_x (NH_3+NH_4^+), Ca^{2+}, K^+, Na^+, Mg^{2+}, Cl^-, RH and T, with the temporal resolution aligned with the sampling periods (from 10:00 AM to 9:00 AM the following day).Input data (excluding RH ≤ 30%) included SO_4^{2-}, TNO_3 (HNO_3 + NO_3^-), TNH_x (NH_3+NH_4^+), Ca^{2+}, K^+, Na^+, Mg^{2+}, Cl^-, RH and T. The concentrations of hydrogen ions in air (H^+_{air}) and ALWC were calculated using the aerosol equilibrium composition system Na^+-K^+-Ca^{2+}-Mg^{2+}-NH_4^+-SO_4^{2-}-NO_3^--Cl^--H_2O H^+_{air} (Fountoukis and Nenes, 2007). pH values were calculated using the following formula:

$$pH = -\log_{10}H^+_{aq} \cong -\log_{10}\frac{1000H^+_{air}}{ALWC_i + ALWC_o} \cong -\log_{10}\frac{1000H^+_{air}}{ALWC_i} \quad (2)$$

$$ALWC_o = \frac{m_{org}\rho_w}{\rho_w}\frac{\kappa_{org}}{\left(\frac{1}{RH}-1\right)} \quad (3)$$

where $ALWC_i$ and $ALWC_o$ refer to the ALWC for inorganic and organic components, respectively.

m_{org} denotes the mass of organic aerosol, ρ_w is the density of water (1.0 g/cm^3), ρ_{org} is the density of organic material (1.4 g/cm^3) (Guo et al., 2015), k_{org} is the hygroscopicity parameter for organic aerosol (0.087) (Chang et al., 2010; Li et al., 2016). The ISORROPIA-II model operated under metastable conditions in the forward mode. Due to the lack of measured data for gaseous HNO_3 and NH_3, TNO_3 was represented solely by NO_3^-. The concentration of NH_3 was simulated based on a linear regression equation proposed by Wei et al. (2023), who used the same data as this study from 2013 to 2020:

$$NH_3 = 19.909 \times RH + 0.559 \times T - 0.35 \times NH_4^+ + 0.123 \times NO_3^- + 2.159 \times Cl^- - 0.224 \times SO_4^{2-} - 154.923 \quad (4)$$

where NO_3^-, SO_4^{2-}, NH_4^+, and Cl^- correspond to their respective concentrations (μg/m^3). To validate the applicability of Equation 4 for annual NH_3 estimation and pH simulation in Zhengzhou, this study utilized both observed NH_3 data (from a Thermo Scientific URG-9000D ambient ion monitor, USA) and calculated NH_3 values derived from Equation 4 at the same monitoring site throughout 2022, inputting them into the thermodynamic model for pH simulation. As shown in Figure S2, pH values calculated from observed and simulated NH_3 exhibit good agreement ($r = 0.97$, $P < 0.01$). Furthermore, NH_3 concentrations modeled by ISORROPIA demonstrate a significant correlation ($r = 0.95$, $P < 0.01$) with that simulated NH_3 by Equation 4. These results collectively demonstrate the reliability of the NH_3 estimation method in this study.

2.2.3 HYSPLIT analysis

Backward trajectories were calculated using the mixed-particle Lagrangian integrated trajectory method (HYSPLIT, https:// www.ready.noaa.gov/HYSPLIT_traj.php). Meteorological input data were from the Global Data Assimilation System (GDAS) with 3D wind vectors, temperature, relative

humidity, geopotential height, surface pressure, and boundary layer diagnostics. 24-h backward trajectories were simulated for air masses above 1000 m above ground level in Zhengzhou. While the surface elevation of Zhengzhou is approximately 100 m above sea level (ASL), setting the height at 1000 m ASL takes into account the minimum altitude needed to traverse the average elevation of the Taihang Mountains (ranging from 1000 to 1500 m ASL). This ensures that the simulated trajectory paths over this topographical barrier are physically realistic.

The Angle Distance algorithm was used to cluster air mass trajectories, enabling the identification of dominant air mass directions and potential pollution sources affecting the study site during different periods. The optimal number of clusters was determined by evaluating the spatial variance (SPVAR) of each trajectory from the cluster mean and the total spatial variance (TSV). The final classification was selected just before the second rapid increase in TSV. The underlying principle is that TSV initially rises sharply during clustering, then increases gradually; however, once the number of clusters reaches a certain threshold, TSV surges again, indicating that the merged clusters are highly dissimilar, marking the end of the classification process. The classification results correspond to the different air mass categories before this final merging step. The mean trajectories of these clusters represent the primary airflow patterns at the target site during the analysis period (Wang et al., 2009). Subsequently, trajectories from two periods, 2013–2018 and 2019–2022, were clustered separately to analyze the variations between the two policy implementation periods.

3 Results and discussion

3.1 Temporal variations in chemical components

Over the past twelve years, the Chinese government implemented the Air Pollution Prevention and Control Action Plans (2013–2018) and the Three-Year Action Plan (2018–2020). The Air Pollution Prevention and Control Action Plan focused on reducing $PM_{2.5}$ concentrations in key regions and aiming to cut $PM_{2.5}$ levels by 10–25% in priority areas over five years. To achieve these goals, it adopted several measures. In terms of industrial restructuring, it mandated the elimination of a large amount of outdated production capacity in industries such as iron/steel and cement to optimize the industrial structure and reduce high-pollution production. For emission standards, it set strict requirements for multiple industrial sectors, especially coal-fired power plants, and gradually introduced ultra-low emission requirements to control pollutants like SO_2, NO_x, and PM. Regarding energy transition, it promoted a shift from coal to cleaner energy sources, including capping coal consumption in certain regions and restricting the construction of small-scale coal-fired boilers. Subsequently, the Three-Year Action Plan was carried out to continue improving air quality with a broader scope of regions under control, further reducing pollutant emissions and enhancing the overall air quality index. The measures included enhanced transportation controls, such as introducing stricter vehicle emission standards (like National VI standards for vehicles) and establishing diesel truck exclusion zones in many cities to reduce emissions from the transportation sector. It also adopted precision governance through grid-based environmental supervision, dividing areas into small grids for more accurate and efficient monitoring of pollution sources. Additionally, it strengthened the legal

and institutional framework by revising relevant laws, such as the Air Pollution Prevention and Control Law, to strengthen legal penalties for environmental violations and implementing an environmental tax system to encourage enterprises to reduce emissions.

The long-term trends in $PM_{2.5}$ concentrations and its chemical components in Zhengzhou from 2011 to 2022 are depicted in Fig. 1, with annual average concentrations listed in Table 1. Correspondingly, the annual average concentration of $PM_{2.5}$ in Zhengzhou decreased from 162 ± 81 μg/m^3 in 2011 to 60 ± 41 μg/m^3 in 2022, representing a reduction of approximately 63%. In particular, the reduction rate reached 72% after 2013. As for chemical components, the largest reductions were observed in SO_4^{2-} (79%), decreasing from 38.0 ± 19.9 μg/m^3 in 2013 to 7.9 ± 4.5 μg/m^3 in 2022, followed by EC (76%). Additionally, the concentrations of NH_4^+ and NO_3^- also significantly decreased by 68% and 56%, respectively. The proportion of each component in $PM_{2.5}$ (Fig. S3) reveals a decrease in SO_4^{2-}, K^+, and Cl^-, indicating effective control measures targeting coal and biomass combustion (Lei et al., 2021). However, the proportions of NO_3^- and OC in $PM_{2.5}$ rose from 11% and 12% in 2013 to 13% and 17% in 2022, respectively, similar to the trend observed in the North China Plain (Wen et al., 2018; Zhai et al., 2019; Li et al., 2023).

3.2 Temporal variations in CM

Notably, there is no clear declining trend in the CM concentration, with a rebound observed during 2020–2022 (Fig. 1i). Furthermore, the proportion of CM in $PM_{2.5}$ exhibits a significant upward trend (Fig. S3). To further analyze its trend, sampling data were divided into three periods corresponding to governmental stages: 2011–2013, when no special control measures were implemented; 2013–2019,

242 coinciding with the implementation of the Air Pollution Prevention and Control Action Plan; and
243 2019–2022, coinciding with the Three-Year Action Plan. During these periods, Henan Province and
244 Zhengzhou City implemented several dust control policies summarized in Table S3. As shown in Fig.
245 2a and 2b, the mass concentration of CM peaked at 14.6 ± 8.3 μg/m^3 in 2013, accounting for 8% of
246 $PM_{2.5}$. To evaluate the inter - annual change trend of CM, the Mann - Kendall method, Sen's slope,
247 and Least - Squares (LS) slope were comprehensively used with the results presented in Table S4.
248 From 2013 to 2019, the CM concentration notably decreased from 14.6 ± 8.3 to 8.5 ± 7.8 μg/m^3, with
249 an annual average decline rate of 0.81 μg/(m^3·year) from LS slope [0.015 μg/(m^3·year) from Sen's
250 slope]. Apart from control measures, the interannual meteorological analysis shows (Fig. S4) WS
251 exhibited a declining trend, with a decrease rate of 43%, while RH showed an increasing trend at a rate
252 of 8% from 2013 to 2019, under which conditions that were unfavorable for dust resuspension (Wang
253 et al., 2013, 2018). Seasonal trends (Fig. S5) reveal significant declines in CM during spring in 2013–
254 2019 with WS decreasing from 2.2 m/s in 2013 to 1.4 m/s in 2019 (Fig. S6) and stable RH (Fig. S7).
255 Similarly, summer CM reductions in 2013–2019 corresponded with WS declines. These patterns
256 suggest spring-summer CM improvements resulted from the synergistic effects of meteorological
257 changes and dust control policies. Conversely, autumn-winter seasons showed limited CM reductions
258 despite comparable WS decreases in 2013–2019, highlighting the need for enhanced dust emission
259 controls in Zhengzhou during these seasons. As for the individual crustal elements in Fig. S8, Ca
260 exhibited the highest average annual decline rate of 33% during 2013–2019, followed by Al. Si showed
261 a less pronounced decline, attributed to its association with soil dust, where control measures for
262 exposed soil are lacking (Zhang et al., 2020). In addition, the Ca^{2+} concentration as depicted in Fig. 2c

decreased from 3.2 ± 2.1 μg/m^3 in 2013 to 2.2 ± 1.1 μg/m^3 in 2019, with an approximate annual average decline rate of 0.32 μg/(m^3·year) from LS slope [4.14E–03 μg/(m^3·year) from Sen's slope] in Table S4, further demonstrating the decline in dust source. It was worth noting that the proportions of CM, Ca, Al, Fe, Si, and Ca^{2+} in $PM_{2.5}$ have shown consecutive annual increases from 2013 to 2019, with CM proportion increasing from 8% in 2013 to 14% in 2019, indicating that CM reduction lagged behind $PM_{2.5}$ reduction efforts in Zhengzhou during this period. Additionally, both concentration and proportion of Ca^{2+} in 2022 (2.2 ± 1.1 μg/m^3 and 14%) were higher than in other cities of China, such as Beijing (1.0 μg/m^3 and 2.8%), Tianjin (0.5 μg/m^3 and 1.4%), and Xiamen (0.48 μg/m^3 and 1.5%) (Shi et al., 2017; Xu et al., 2025; Zhang et al., 2021). These results indicate that CM remained an important component of $PM_{2.5}$ in Zhengzhou City.

During 2019–2022, both CM and Ca^{2+} concentrations exhibited significant rebounds, with annual growth rates of 0.24 and 0.4 μg/(m^3·year) from LS slope [5.80E–03 and 5.42E–03 μg/(m^3·year) from Sen's slope], respectively, and their proportions increased from 14% and 2% in 2019 to 22% and 5% in 2022. CM concentrations rebounded in all seasons, particularly in winter (Fig. S5). Changes in meteorological conditions may be a significant factor contributing to these concentration rebounds, accompanied by the average WS increased by 0.14 m/s and RH decreased by 7% from 2020 to 2022 (Fig. S4, S6, and S7), facilitating dust resuspension. Furthermore, the lack of more effective dust control measures, as indicated by the absence of significant changes in the dust control policies from the Air Pollution Prevention and Control Action Plan and Three-Year Action Plan, may be another important factor contributing to the rebound of dust.

3.3 Sources of CM

Elemental ratios were employed to characterize the sources of CM, with the Ca/Al ratio widely recognized as a reliable indicator of sandy origin (Zhang et al., 2017). In addition, significant variations in Ca/Si ratios (Table S5) were observed among different dust sources (Road, Construction, Piles, Soil). Fig. 3a illustrates the trend in Ca/Si ratios from 2011 to 2022. After 2013, Ca/Si ratios showed a declining trend annually, with the average ratio decreasing from a peak of 1.6 in 2016 to a lowest of 0.4 in 2022. Compared with Ca/Si ratios from different types of dust sources, the effect of road and construction dust on CM has gradually decreased. This may be attributed to the implementation of dust control measures such as enclosure, shielding, and dust suppression at construction and demolition sites, as well as dust control on ground surfaces and roads (Table S5). During 2019–2022, the average Ca/Si ratio remained below 1, with a mean of 0.4 in 2022, indicating that soil dust predominantly contributed to CM. Currently, measures for controlling soil-suspended dust are limited, primarily relying on long-term strategies such as afforestation and increasing urban green coverage, thus requiring a longer process and sustained investment.

Sand dust transport serves as a significant source of CM in the North China Plain (Zhang et al., 2024). The Ca/Al ratio from 2016 to 2022 (Fig. 3b) shows minimal variation, with annual averages ranging between 1.5 and 2.5, indicating no significant changes in the source regions of sand. The transport trajectories reveal that the predominant pathways for long-distance transport of sand dust originated from Inner Mongolia, passing through Shaanxi and Shanxi provinces. Compared to 2013–2018 (45%), the influence of long-distance transport decreased to 25% during 2019–2022. In contrast, local transport within Henan province and short-distance transport from Shandong province showed a

304 noticeable increase. These findings suggest that the rebound in CM concentrations during 2019–2022
305 in Zhengzhou might be responsible for the resuspension of surrounding soil dust.

306 ## 3.4 Long-term trend of particle pH

307 Are shown in Fig. 4 and Table S4, pH values showed a clearly increasing trend after 2014. From
308 2013 to 2019, the annual pH increased by 0.11 units from the LS slope [9.15E–04 units from Sen's
309 slope], reaching a maximum median value of 4.45 (Mean: 4.35) in 2018. Note that the annual average
310 growth rate of pH values increased to 0.21 units from LS slope [2.93E–03 units from Sen's slope] from
311 2019 to 2022, with a maximum median value of 4.42 (Mean: 4.51) in 2022. Seasonally, pH values
312 showed increasing trends in spring, summer, and autumn, and notably increased in winter from 2020
313 to 2022 (Fig. S9). The increasing trend in pH values observed in this study is similar to the findings in
314 Beijing (Song et al., 2019; Xie et al., 2020), presumably attributable to the comparable chemical
315 composition trends and meteorological conditions. In contrast, Shanghai and Hong Kong display
316 divergent trends (Nah et al., 2023; Zhou et al., 2022). This disparity might be ascribed to the stronger
317 buffering effect exerted by NH_3 and dust in Zhengzhou than marine aerosols (Na^+/Cl^-) in these coastal
318 cities (Shi et al., 2017; Liu et al., 2019). Moreover, the relatively higher temperatures and more
319 abundant rainfall in Shanghai and Hong Kong could also contribute to the distinct trends observed in
320 their pH values.

321 Sensitivity analyses were conducted to explore the dominant factors driving the elevated particle
322 pH in Zhengzhou by giving a range for one parameter (i.e., TNH_x) and average values for other
323 parameters (i.e., SO_4^{2-}, NO_3^-, Na^+, Cl^-, Ca^{2+}, K^+, Mg^{2+}, RH, and T) input into the ISORROPIA-II model.

Are shown in Fig. S10, particle pH increases with the cation concentrations (e.g., TNH_x, K^+, Ca^{2+}, Mg^{2+}, and Na^+) and decreases with anions concentrations (e.g., SO_4^{2-} and NO_3^-). Additionally, RH does not significantly affect pH, whereas an increase in T leads to a noticeable decrease in particle pH.

Based on the sensitivity analysis curves, the pH values corresponding to a variable in different years were calculated according to the average values of this variable in different years (Table S6). The difference in pH values of this variable between two adjacent years was defined as ΔpH which is illustrated in Fig. 5. According to Equation (2), in addition to H^+ concentration, particle pH is primarily influenced by the dilution effect of ALWC. Moreover, ALWC affects the gas-particle partitioning of semi-volatile compounds, thereby influencing particle acidity (Zuend et al., 2010; Zuend and Seinfeld, 2012). As shown in Fig.5 and Table S6, only in 2015, 2019, and 2020 did the increases in ALWC concentration (17.6 μg/m³, 4.1 μg/m³, and 11.6 μg/m³, respectively) lead to pH increases of 0.22, 0.06, and 0.14 units. This clearly cannot fully explain the significant pH increase in Zhengzhou since 2013. Notably, since 2013, H^+ concentration has shown a decreasing trend. Particularly, H^+ concentrations decreased by 7.6×10^{-6}, 11.2×10^{-6}, and 7.2×10^{-6} mol/L in 2013, 2015, and 2017, respectively, leading to pH increases of 0.21, 0.36, and 0.42 units. After 2019, a continuous decline in H^+ concentration was observed for three consecutive years, resulting in pH increases of 0.21, 0.13, and 0.2 units in 2020, 2021, and 2022, respectively. These findings indicate that the increase in pH from 2019 to 2022 in Zhengzhou was primarily driven by the reduction in H^+ concentration.

The concentration of H^+ in the aerosol liquid phase is influenced by both chemical composition and meteorological conditions. To further understand the factors affecting ΔpH, we analyzed the variations in $PM_{2.5}$ chemical components and meteorological parameters. Results indicate that the

345 decline in SO_4^{2-} from 2013 to 2018 was the primary cause of the increase in particle pH, as it decreased
346 H^+ and ALWC concentrations (Fig. S11) in aerosol (Ding et al., 2019; Zhang et al., 2021). The average
347 SO_4^{2-} concentration decreased by 14.6 and 5.3 μg/m^3, resulting in a pH increase of 0.43 and 0.35 units
348 from 2013 to 2014 and 2016 to 2017, respectively, which was comparable to an increased rate of 0.3
349 units in East Asia due to SO_2 emission controls since 2016 (Karydis et al., 2021). As another acidic
350 ion, the decrease in nitrate concentration did not significantly contribute to the pH increases, consistent
351 with findings from Ding et al. (2019) and Zhang et al. (2021). This is primarily because NO_3^- declined
352 more slowly compared to sulfate ions and exceeded sulfate concentrations after 2016, under which
353 conditions that nitrate-rich particles can absorb twice the amount of water that sulfate-rich particles,
354 leading to an increase in ALWC concentration and inhibiting pH decline (Lin et al., 2020; Xie et al.,
355 2020). On the other hand, increases in particle pH in 2015 and 2018 were notably influenced by
356 changes in TNH_x with concentrations increased by 5.5 and 1.3 μg/m^3, respectively. Increased TNH_x
357 concentrations could react with SO_4^{2-} or NO_3^- and consume a substantial amount of H^+, thereby raising
358 particulate matter pH values (Seinfeld et al., 1998; Zhang et al., 2021). Substantial decreases in T in
359 2015 (4.2℃), 2017 (4.9℃), and 2018 (2.8℃), favoring NH_3 partitioning into the particle phase and
360 reducing H^+ concentrations, drove increases in particle pH (Tao and Murphy, 2019).

361 During the period from 2020 to 2022, the influence of SO_4^{2-} on particle pH gradually decreased,
362 with a decrease in concentration from 0.3 to 2.3 μg/m^3 (Table S6) only bringing about a pH decrease
363 of 0.03 to 0.14 (Fig. 5). Moreover, a rebound in SO_4^{2-} concentration to 7.9 ± 4.5 μg/m^3 in 2022 even
364 resulted in a decrease of 0.11 units in pH instead. On the other hand, TNHx began to show a slight
365 annual decline (0.9 to 2.2 μg/m^3), resulting in a significant decrease in pH (0.21–0.35). Consequently,

366 the increase in pH values was closely related to the rise in Ca^{2+} concentration. Ca^{2+} is less volatile and
367 competes preferentially with NH_3 to neutralize anions such as SO_4^{2-} to form insoluble $CaSO_4$, which
368 precipitates from the aerosol aqueous phase (Ding et al., 2019; Karydis et al., 2021), thereby reducing
369 H^+ concentrations (Fig. S11) and subsequently lowering particle acidity. Specifically, increases of 0.7
370 and 0.5 μg/m^3 in Ca^{2+} concentrations led to pH increases of 0.13 and 0.09 units in 2020 and 2022,
371 respectively, making Ca^{2+} a primary controlling factor for pH elevation..

372 # 4 Conclusions

373 The annual average $PM_{2.5}$ concentration in Zhengzhou decreased from 212.4 ± 101.5 μg/m^3 in
374 2013 to 59.5 ± 41.2 μg/m^3 in 2022, with the largest reduction in SO_4^{2-}. As for CM, their concentrations
375 notably decreased from 2013 to 2019, because of effective dust control measures, as well as decreased
376 wind speed and increased relative humidity. However, the proportions of CM in $PM_{2.5}$ have shown
377 consecutive annual increases. In addition, CM concentrations and their proportions increased
378 significantly during 2019–2022, which might be responsible for the resuspension of surrounding soil
379 dust. Correspondingly, the annual pH increased by 0.11 units from 2013 to 2019 mainly due to the
380 decline in SO_4^{2-}, increased TNH_x, or decreased temperature. During the period from 2020 to 2022, the
381 annual average growth rate of pH values increased to 0.21 units from 2019 to 2022, which was
382 determined by the rise in Ca^{2+} concentration.

5 Implication

Control measures implemented by the Chinese government have proven effective in reducing dust, but this study reveals that the crustal materials in $PM_{2.5}$ rebounded after 2019. This phenomenon is not unique to Zhengzhou, as major cities in the North China Plain have also experienced a pronounced upward trend in coarse particles after 2019 (Fig. S12). Thus, crustal materials persist as a substantial constituent of atmospheric aerosols in North China, sustaining elevated particle pH levels. Extensive research has established that heightened particle pH inhibits nitrate reduction in aerosols (Ding et al., 2019; Lin et al., 2020; Wen et al., 2018), particularly significant given nitrate's predominant role in haze formation within this region. Notably, while moderately acidic aerosols demonstrate reduced health impacts, particles with pH < 3 exhibit substantially greater health risks (Shi et al., 2019). Consequently, future environmental management strategies must prioritize real-time assessment of regulatory impacts on particle acidity. This necessitates an integrated approach that simultaneously addresses acidic precursors, alkaline precursors, and crustal material contributions to atmospheric acid chemistry.

Data availability

All the data presented in this article can be accessed through https://doi.org/10.5281/zenodo.14032007 (Zhang, 2024).

Supporting Information

Additional data, figures, and tables, some of which are referenced directly within the manuscript, and detailed descriptions of field measurements and samples.

Author contributions

S.W. designed this study. H.Z. and Z.D. analyzed the data and prepared the manuscript with the contributions of all coauthors. X.L. conducted measurements. R.Z. provided funding acquisition. All authors have read and agreed to the published version of the manuscript.

Competing interests

The authors declare that they have no conflict of interest.

Acknowledgment

This work was supported by the National Key Research and Development Program of China (No. 2024YFC3713701), the China Postdoctoral Science Foundation (2023 M733220), the Zhengzhou $PM_{2.5}$ and O_3 Collaborative Control and Monitoring Project (20220347 A), and the National Key R&D Program of China No. 2017YFC0212400.

Funding Sources

This work was supported by the National Key Research and Development Program of China (No. 2024YFC3713701), the China Postdoctoral Science Foundation (2023 M733220), the Zhengzhou $PM_{2.5}$ and O_3 Collaborative Control and Monitoring Project (20220347 A), and the National Key Research and Development Program of China (No. 2017YFC0212400).

References

Battaglia, M. A.; Douglas, S.; Hennigan, C.: Effect of the urban heat island on aerosol pH, Environ. Sci. Technol., 51, 13095–13103, https://doi.org/10.1021/acs.est.7b02786, 2017.

Chang, R. Y. W.; Slowik, J. G.; Shantz, N. C.; Vlasenko, A.; Liggio, J.; Sjostedt, S. J.; Leaitch, W. R.; Abbatt, J. P. D. The hygroscopicity parameter (κ) of ambient organic aerosol at a field site subject to biogenic and anthropogenic influences: relationship to degree of aerosol oxidation. Atmos. Chem. Phys., 10, 5047–5064, https://doi.org/10.5194/acp-10-5047-2010, 2010.

Ding, J., Zhao, P., Su, J., Dong, Q., Du, X., and Zhang, Y.: Aerosol pH and its driving factors in Beijing, Atmos. Chem. Phys., 19, 7939–7954, https://doi.org/10.5194/acp-19-7939-2019, 2019.

Dong, J., Li, B., Li, Y., Zhou, R., Gan, C., Zhao, Y., Liu, R., Yang, Y., Wang, T., and Liao, H.: Atmospheric ammonia in China: Long-term spatiotemporal variation, urban-rural gradient, and influencing factors, Sci. Total Environ., 883, 163733, https://doi.org/10.1016/j.scitotenv.2023.163733, 2023.

Fountoukis, C and Nenes, A.: ISORROPIA II: a computationally efficient thermodynamic equilibrium model for K^+ - Ca^{2+} - Mg^{2+} - NH_4^+ - Na^+ - SO_4^{2-} - NO_3^- - Cl^- - H_2O aerosols, Atmos. Chem. Phys., 7, 4639–4659, https://doi.org/10.5194/acp-7-4639-2007, 2007.

Guo, H., Sullivan, A. P., Campuzano-Jost, P., Schroder, J. C., Lopez-Hilfiker, F. D., Dibb, J. E., Jimenez, J. L., Thornton, J. A., Brown, S. S., Nenes, A., and Weber, R. J.: Fine particle pH and the

partitioning of nitric acid during winter in the northeastern United States, J. Geophys. Res. Atmos., 121, 10,355–310,376, https://doi.org/10.1002/2016JD025311, 2016.

Guo, H., Xu, L., Bougiatioti, A., Cerully, K. M., Capps, S. L., Hite Jr, J. R., Carlton, A. G., Lee, S. H., Bergin, M. H., Ng, N. L., Nenes, A., and Weber, R. J.: Fine-particle water and pH in the southeastern United States, Atmos. Chem. Phys., 15, 5211–5228, https://doi.org/10.5194/acp-15-5211-2015, 2015.

Heald, C.; Collett, J. J.; Lee, T.; Benedict, K.; Schwandner, F.; Li, Y.; Clarisse, L.; Hurtmans, D. R.; Van, D. M.; Clerbaux, C.; Coheur, P. F., Philip, S.; Martin, R. V.; Pye, T.: Atmospheric ammonia and particulate inorganic nitrogen over the United States, Atmos. Chem. Phys., 12, 10295–10312, https://doi.org/10.5194/acp-12-10295-2012, 2012.

Huang, X., Song, Y., Li, M., Li, J., Huo, Q., Cai, X., Zhu, T., Hu, M., and Zhang, H.: A high-resolution ammonia emission inventory in China, Global. Biogeochem. Cy., 26, GB1030, https://doi.org/10.1029/2011GB004161, 2012.

Jiang, N.; Duan, S.; Yu, X.; Zhang, R.; Wang, K. Comparative major components and health risks of toxic elements and polycyclic aromatic hydrocarbons of $PM_{2.5}$ in winter and summer in Zhengzhou: Based on three-year data. Atmos. Res., 213, 173–184, https://doi.org/10.1016/j.atmosres.2018.06.008, 2018.

Karydis, V. A., Tsimpidi, A. P., Pozzer, A., and Lelieveld, J.: How alkaline compounds control atmospheric aerosol particle acidity, Atmos. Chem. Phys., 21, 14983–15001, https://doi.org/10.5194/acp-21-14983-2021, 2021.

Kim, Y., Park, O., Park, S. H., Kim, M. J., Kim, J.-J., Choi, J.-Y., Lee, D., Cho, S., and Shim, S.: $PM_{2.5}$ pH estimation in Seoul during the KORUS-AQ campaign using different thermodynamic models, Atmos. Environ., 268, 118787, https://doi.org/10.1016/j.atmosenv.2021.118787, 2022.

Lei, L., Zhou, W., Chen, C., He, Y., Li, Z., Sun, J., Tang, X., Fu, P., Wang, Z., and Sun, Y.: Long-term characterization of aerosol chemistry in cold season from 2013 to 2020 in Beijing, China, Environ. Pollut., 268, 115952, https://doi.org/10.1016/j.envpol.2020.115952, 2021.

Li, C.; Hu, Y.; Chen, J.; Ma, Z.; Ye, X.; Yang, X.; Wang, L.; Wang, X.; Mellouki, A. Physiochemical

properties of carbonaceous aerosol from agricultural residue burning: Density, volatility, and hygroscopicity. Atmos. Environ., 140, 94–105, https://doi.org/10.1016/j.atmosenv.2016.05.052, 2016.

Li, W., Xu, L., Liu, X., Zhang, J., Lin, Y., Yao, X., Gao, H., Zhang, D., Chen, J., Wang, W., Harrison, R. M., Zhang, X., Shao, L., Fu, P., Nenes, A., and Shi, Z.: Air pollution-aerosol interactions produce more bioavailable iron for ocean ecosystems, Sci. Adv., 3, e1601749, https://doi.org/10.1126/sciadv.1601749, 2017.

Li, Y., Lei, L., Sun, J., Gao, Y., Wang, P., Wang, S., Zhang, Z., Du, A., Li, Z., Wang, Z., Kim, J. Y., Kim, H., Zhang, H., and Sun, Y.: Significant reductions in secondary aerosols after the Three-Year Action Plan in Beijing summer, Environ. Sci. Technol., 57, 15945–15955, https://doi.org/10.1021/acs.est.3c02417, 2023.

Lin, Y., Zhang, Y., Fan, M, and Bao, M.: Heterogeneous formation of particulate nitrate under ammonium-rich regimes during the high-$PM_{2.5}$ events in Nanjing, China, Atmos. Chem. Phys., 20, 3999–4011, https://doi.org/10.5194/acp-20-3999-2020, 2020.

Liu, M.; Huang, X.; Song, Y.; Tang, J.; Cao, J.; Zhang, X.; Zhang, Q.; Wang, S.; Xu, T.; Kang, L.; Gai, X.; Zhang, H.; Yang, F.; Wang, H.; Yu, J.; Lau, A.; He, L.; Huang, X.; Duan, L.; Ding, A.; Xue, L.; Gao, J.; Liu, B.; Zhu, T. Ammonia emission control in China would mitigate haze pollution and nitrogen deposition, but worsen acid rain. Proc. Natl. Acad. Sci., 116, 7760–7765, https://doi.org/10.1073/pnas.1814880116, 2019.

Liu, Z., Gao, W., Yu, Y., Hu, B., Xin, J., Sun, Y., Wang, L., Wang, G., Bi, X., Zhang, G., Xu, H., Cong, Z., He, J., Xu, J., and Wang, Y.: Characteristics of $PM_{2.5}$ mass concentrations and chemical species in urban and background areas of China: emerging results from the CARE-China network, Atmos. Chem. Phys., 18, 8849-8871, https://doi.org/10.5194/acp-18-8849-2018, 2018.

Mao, I., Lin, C., Lin, C., Chen, Y., Sung, F., and Chen, M.: Exposure of acid aerosol for schoolchildren in metropolitan Taipei, Atmos. Environ., 43, 5622–5629, https://doi.org/10.1016/j.atmosenv.2009.07.054, 2009.

Masiol, M., Squizzato, S., Formenton, G., Khan, M. B., Hopke, P. K., Nenes, A., Pandis, S. N., Tositti,

L., Benetello, F., Visin, F., and Pavoni, B.: Hybrid multiple-site mass closure and source apportionment of $PM_{2.5}$ and aerosol acidity at major cities in the Po Valley, Sci. Total Environ., 704, 135287, https://doi.org/10.1016/j.scitotenv.2019.135287, 2020.

MEP (Ministry of Environment Protection), 2023. https://www.mee.gov.cn/ywdt/hjywnews/202406/t20240605_1075031.shtml, Accessed date:5 June 2024.

Nah, T., Lam, Y. H., Yang, J., and Yang, L.: Long-term trends and sensitivities of $PM_{2.5}$ pH and aerosol liquid water to chemical composition changes and meteorological parameters in Hong Kong, South China: Insights from 10-year records from three urban sites, Atmos. Environ., 302, https://doi.org/10.1016/j.atmosenv.2023.119725, 2023.

Nenes, A., Pandis, S. N., Kanakidou, M., Russell, A. G., Song, S., Vasilakos, P., and Weber, R. J.: Aerosol acidity and liquid water content regulate the dry deposition of inorganic reactive nitrogen, Atmos. Chem. Phys., 21, 6023–6033, https://doi.org/10.5194/acp-21-6023-2021, 2021.

Pinder, R., Adams, P., and Pandis, S.: Ammonia emission controls as a cost-effective strategy for reducing atmospheric particulate matter in the eastern United States, Environ. Sci. Technol., 41, 380–386, https://doi.org/10.1021/es060379a, 2007.

Pinder, R., Gilliland, A., and Dennis, R.: Environmental impact of atmospheric NH_3 emissions under present and future conditions in the eastern United States, Geophys. Res. Lett., 35, 28, https://doi.org/10.1029/2008gl033732, 2008.

Pye, H. O. T.; Nenes, A.; Alexander, B.; Ault, A. P.; Barth, M. C.; Clegg, S. L.; Collett Jr, J. L.; Fahey, K. M.; Hennigan, C. J.; Herrmann, H.; Kanakidou, m.; Kelly, J. T.; Ku, L.; McNeill, V. F.; Riemer, N.; Schaefer, T.; Shi, G.; Tilgner, A.; Walker, J.T.; Wang, T.; Weber, R.; Xing, J.; Zaveri, R. A.; Zuend, A. The acidity of atmospheric particles and clouds. Atmos. Chem. Phys., 20, 4809–4888, https://doi.org/10.5194/acp-20-4809-2020, 2020.

Rengarajan, R., Sudheer, A. K., and Sarin, M. M.: Aerosol acidity and secondary organic aerosol formation during wintertime over urban environment in western India, Atmos. Environ., 45, 1940–1945, https://doi.org/10.1016/j.atmosenv.2011.01.026, 2011.

Seinfeld, J. H., Pandis, S. N., and Noone, K. J.: Atmospheric chemistry and physics: From air pollution

518 to climate change, Phys. Today., 51, 88–90, https://doi.org/10.1063/1.882420, 1998.
519 Sharma, B., Jia, S., Polana, A. J., Ahmed, M. S., Haque, R. R., Singh, S., Mao, J., and Sarkar, S.:
520 Seasonal variations in aerosol acidity and its driving factors in the eastern Indo-Gangetic Plain:
521 A quantitative analysis, Chemosphere., 305, 135490,
522 https://doi.org/10.1016/j.chemosphere.2022.135490, 2022.
523 Shi, G., Xu, J., Peng, X., Xiao, Z., Chen, K., Tian, Y., Guan, X., Feng, Y., Yu, H., Nenes, A., and Russell,
524 A. G.: pH of aerosols in a polluted atmosphere: source contributions to highly acidic aerosol,
525 Environ. Sci. Technol., 51, 4289–4296, https://doi.org/10.1021/acs.est.6b05736, 2017.
526 Shi, X., Nenes, A., Xiao, Z., Song, S., Yu, H., Shi, G., Zhao, Q., Chen, K., Feng, Y., and Russell, A.
527 G.: High-resolution data sets unravel the effects of sources and meteorological conditions on
528 nitrate and its gas-particle partitioning, Environ. Sci. Technol., 53, 3048–3057,
529 https://doi.org/10.1021/acs.est.8b06524, 2019.
530 Song, S., Nenes, A., Gao, M., Zhang, Y., Liu, P., Shao, J., Ye, D., Xu, W., Lei, L., Sun, Y., Liu, B.,
531 Wang, S., and McElroy, M. B.: Thermodynamic modeling suggests declines in water uptake and
532 acidity of inorganic aerosols in Beijing winter haze events during 2014/2015–2018/2019, Environ.
533 Sci. Technol. Lett., 6, 752–760, https://doi.org/10.1021/acs.estlett.9b00621, 2019.
534 Su, H., Cheng, Y., and Pöschl, U.: New Multiphase Chemical Processes Influencing Atmospheric
535 Aerosols, Air Quality, and Climate in the Anthropocene, Acc. Chem. Res., 53, 2034–2043,
536 https://doi.org/10.1021/acs.accounts.0c00246, 2020.
537 Surratt, J. D., Chan, A. W. H., Eddingsaas, N. C., Chan, M., Loza, C. L., Kwan, A. J., Hersey, S. P.,
538 Flagan, R. C., Wennberg, P. O., and Seinfeld, J. H.: Reactive intermediates revealed in
539 secondary organic aerosol formation from isoprene, Proc. Natl. Acad. Sci., 107, 6640–6645,
540 https://doi.org/10.1073/pnas.0911114107, 2010.
541 Tao, Y. and Murphy, J. G.: The sensitivity of $PM_{2.5}$ acidity to meteorological parameters and chemical
542 composition changes: 10-year records from six Canadian monitoring sites, Atmos. Chem. Phys.,
543 19, 9309–9320, https://doi.org/10.5194/acp-19-9309-2019, 2019.
544 Tian, Y.; Chen, G.; Wang, H.; Huang-Fu, Y.; Shi, G.; Han, B.; and Feng, Y.: Source regional

contributions to $PM_{2.5}$ in a megacity in China using an advanced source regional apportionment method. Chemosphere., 147, 256–263, https://doi.org/10.1016/j.chemosphere.2015.12.132, 2016.

Tremper, A.; Font, A.; Priestman, M.; Hamad, S.; Chung, T.; Pribadi, A.; Brown, R.; Goddard, S.; Grassineau, N.; Petterson, K.; Kelly, F.; Green, D.: Field and laboratory evaluation of a high time resolution x-ray fluorescence instrument for determining the elemental composition of ambient aerosols, Atmos. Meas. Tech., 11, 3541–3557, https://doi.org/10.5194/amt-11-3541-2018, 2018.

Wang, C., Yin, S., Bai, L., Zhang, X., Gu, X., Zhang, H., Lu, Q., and Zhang, R.: High-resolution ammonia emission inventories with comprehensive analysis and evaluation in Henan, China, 2006–2016, Atmos. Environ., 193, 11–23, https://doi.org/10.1016/j.atmosenv.2018.08.063, 2018.

Wang, G., Chen, J., Xu, J., Yun, L., Zhang, M., Li, H., Qin, X., Deng, C., Zheng, H., Gui, H., Liu, J., and Huang, K.: Atmospheric processing at the Sea-Land interface over the South China Sea: Secondary aerosol formation, aerosol acidity, and role of sea salts, J. Geophys. Res. Atmos., 127, https://doi.org/10.1029/2021jd036255, 2022.

Wang, L., Du, H., Chen, J., Zhang, M., Huang, X., Tan, H., Kong, L., and Geng, F.: Consecutive transport of anthropogenic air masses and dust storm plume: Two case events at Shanghai, China, Atmos. Res., 127, 22–33, https://doi.org/10.1016/j.atmosres.2013.02.011, 2013.

Wang, S., Yin, S., Zhang, R., Yang, L., Zhao, Q., Zhang, L., Yan, Q., Jiang, N., and Tang, X.: Insight into the formation of secondary inorganic aerosol based on high-time-resolution data during haze episodes and snowfall periods in Zhengzhou, China, Sci. Total Environ., 660, 47–56, https://doi.org/10.1016/j.scitotenv.2018.12.465, 2019.

Wang, S.; Wang, L.; Li, Y.; Wang, C.; Wang, W.; Yin, S.; Zhang, R.; Effect of ammonia on fine-particle pH in agricultural regions of China: comparison between urban and rural sites, Atmos. Chem. Phys., 20, 2719–2734, https://doi.org/10.5194/acp-20-2719-2020, 2020.

Wang, Y., Zhang, X., and Draxler, R.: TrajStat: GIS-based software that uses various trajectory statistical analysis methods to identify potential sources from long-term air pollution measurement data, Environ. Model. Softw., 24, 938–939, https://doi.org/10.1016/j.envsoft.2009.01.004, 2009.

572 Wang, Z., Pan, X., Uno, I., Chen, X., Yamamoto, S., Zheng, H., Li, J., and Wang, Z.: Importance of
573 mineral dust and anthropogenic pollutants mixing during a long–lasting high PM event over East
574 Asia, Environ. Pollut., 234, 368–378, https://doi.org/10.1016/j.envpol.2017.11.068, 2018.
575 Weber, R.; Guo, H.; Russell, A.; Nenes, A.: High aerosol acidity despite declining atmospheric sulfate
576 concentrations over the past 15 years, Nature Geoscience., 9, 282–285,
577 https://doi.org/10.1038/ngeo2665, 2016.
578 Wei, Y.; Wang, S.; Jiang, N.; Zhang, R.; and Hao, Q. Comparative multi-model study of $PM_{2.5}$ acidity
579 trend changes in ammonia-rich regions in winter: Based on a new ammonia concentration
580 assessment method, J. Hazard., 458, 15, https://doi.org/10.1016/10.1016/j.jhazmat.2023.131970,
581 2023.
582 Wen, L., Xue, L., Wang, X., Xu, C., Chen, T., Yang, L., Wang, T., Zhang, Q., and Wang, W.:
583 Summertime fine particulate nitrate pollution in the North China Plain: increasing trends,
584 formation mechanisms and implications for control policy, Atmos. Chem. Phys., 18, 11261–
585 11275, https://doi.org/10.5194/acp-18-11261-2018, 2018.
586 Wexler, A. S. and Seinfeld, J. H.: Second-generation inorganic aerosol model, Atmos. Environ., Part
587 A. General Topics, 25, 2731-2748, https://doi.org/10.1016/0960-1686(91)90203-J, 1991.
588 Xie, Y., Wang, G., Wang, X., Chen, J., Chen, Y., Tang, G., Wang, L., Ge, S., Xue, G., Wang, Y., and
589 Gao, J.: Nitrate-dominated $PM_{2.5}$ and elevation of particle pH observed in urban Beijing during
590 the winter of 2017, Atmos. Chem. Phys., 20, 5019–5033, https://doi.org/10.5194/acp-20-5019-
591 2020, 2020.
592 Xu, K., Yin, L., Chen, Q., Liao, D., Ji, X., Zhang, K., Wu, Y., Xu, L., Li, M., Fan, X., Zhang, F., Huang,
593 Z., Chen, J., and Hong, Y.: Quantitative analysis of influencing factors to aerosol pH and its
594 responses to $PM_{2.5}$ and O_3 pollution in a coastal city, J. Environ. Sci., 151, 284–297,
595 https://doi.org/10.1016/j.jes.2024.03.044, 2025.
596 Yu, F., Yan, Q., Jiang, N., Su, F., Zhang, L., Yin, S., Li, Y., Zhang, R., and Chen, L.: Tracking pollutant
597 characteristics during haze events at background site Zhongmu, Henan Province, China, Atmos.
598 Pollut. Res., 8, 64–73, https://doi.org/10.1016/j.apr.2016.07.005, 2017.

599 Zhai, S.; Jacob, DJ.; Wang, X.; Shen, L.; Li, K.; Zhang, Y.; Gui, K.; Zhao, T.; Liao, H. Fine particulate
600 matter ($PM_{2.5}$) trends in China, 2013–2018: separating contributions from anthropogenic
601 emissions and meteorology, Atmos. Chem. Phys., 19, 11031–11041, https://doi.org/10.5194/acp-
602 19-11031-2019, 2019.
603 Zhang, B., Shen, H., Liu, P., Guo, H., Hu, Y., Chen, Y., Xie, S., Xi, Z., Skipper, T. N., and Russell, A.
604 G.: Significant contrasts in aerosol acidity between China and the United States, Atmos. Chem.
605 Phys., 21, 8341–8356, https://doi.org/10.5194/acp-21-8341-2021, 2021.
606 Zhang, G., Ding, C., Jiang, X., Pan, G., Wei, X., and Sun, Y.: Chemical compositions and sources
607 contribution of atmospheric particles at a typical steel industrial urban site, Sci. Rep., 10, 7654,
608 https://doi.org/10.1038/s41598-020-64519-x, 2020.
609 Zhang, Z., Dong, Z., Zhang, C., Qian, G., and Lei, C.: The geochemical characteristics of dust material
610 and dust sources identification in northwestern China, J. Geochem. Explor., 175, 148–155,
611 https://doi.org/10.1016/j.gexplo.2016.11.006, 2017.
612 Zhang, Z., Kuang, Z., Yu, C., Wu, D., Shi, Q., Zhang, S., Wang, Z., and Liu, D.: Trans–boundary dust
613 transport of dust storms in Northern China: A study utilizing ground–based lidar network and
614 CALIPSO satellite, Remote sens.,16, 1196, https://doi.org/10.3390/rs16071196, 2024.
615 Zheng, G., Su, H., and Cheng, Y.: Revisiting the key driving processes of the decadal trend of aerosol
616 acidity in the U.S, Acs. Environ. Au., 2, 346–353, https://doi.org/10.1021/acsenvironau.1c00055,
617 2022.
618 Zheng, G., Su, H., Wang, S., Andreae, M. O., Pöschl, U., and Cheng, Y.: Multiphase buffer theory
619 explains contrasts in atmospheric aerosol acidity, Science., 369, 1374–1377,
620 https://doi.org/10.1126/science.aba3719, 2020.
621 Zhou, M., Zheng, G., Wang, H., Qiao, L., Zhu, S., Huang, D., An, J., Lou, S., Tao, S., Wang, Q., Yan,
622 R., Ma, Y., Chen, C., Cheng, Y., Su, H., and Huang, C.: Long-term trends and drivers of aerosol
623 pH in eastern China, Atmos. Chem. Phys., 22, 13833–13844, https://doi.org/10.5194/acp-22-
624 13833-2022, 2022.
625 Zhou, W., Gao, M., He, Y., Wang, Q., Xie, C., Xu, W., Zhao, J., Du, W., Qiu, Y., Lei, L., Fu, P., Wang,

Z., Worsnop, D. R., Zhang, Q., and Sun, Y.: Response of aerosol chemistry to clean air action in Beijing, China: Insights from two-year ACSM measurements and model simulations, Environ Pollut., 255, 113345, https://doi.org/10.1016/j.envpol.2019.113345, 2019.

Zuend, A. and Seinfeld, J. H.: Modeling the gas-particle partitioning of secondary organic aerosol: the importance of liquid-liquid phase separation, Atmos. Chem. Phys., 12, 3857–3882, https://doi.org/10.5194/acp-12-3857-2012, 2012.

Zuend, A., Marcolli, C., Peter, T., and Seinfeld, J. H.: Computation of liquid-liquid equilibria and phase stabilities: implications for RH-dependent gas/particle partitioning of organic-inorganic aerosols, Atmos. Chem. Phys., 10, 7795–7820, https://doi.org/10.5194/acp-10-7795-2010, 2010.

Figures

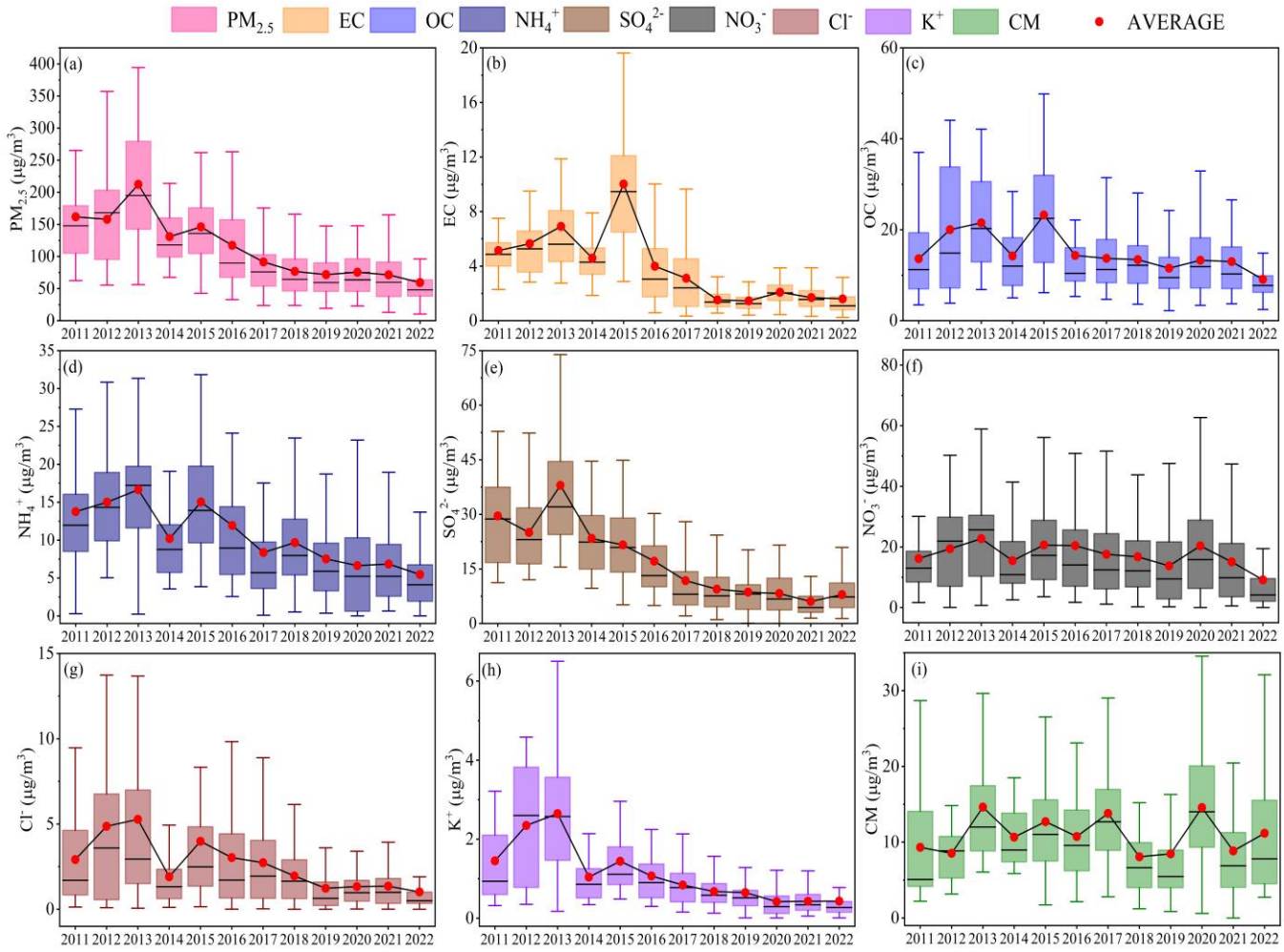

Figure 1. Long-term trends in the concentrations of $PM_{2.5}$ and its chemical components in from 2011 to 2022 in Zhengzhou. Box plots depict annual averages (red dots) and medians (black lines), the top, middle, and bottom lines represent the 75, 50, and 25 percentiles of statistical data, respectively, and the upper and lower whiskers represent the 90 and 10 percentiles of statistical data, respectively.

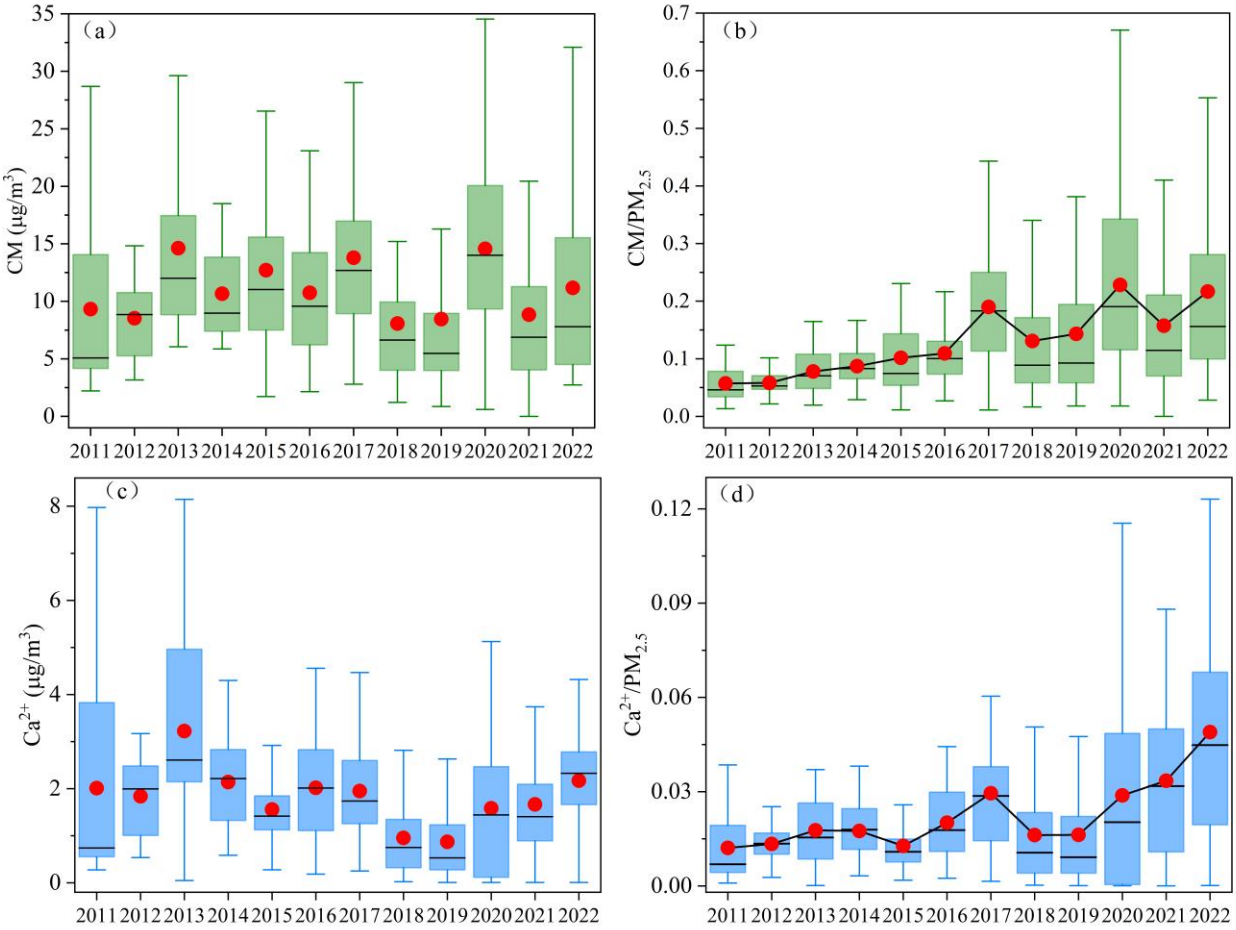

Figure 2. (a) and (c) Long-term trends in CM and Ca^{2+} concentrations in Zhengzhou from 2011 to 2022, respectively. Box plots depict annual averages (red dots) and medians (black lines). (b) and (d) Long-term trends in the proportions of CM and Ca^{2+} in $PM_{2.5}$, respectively.

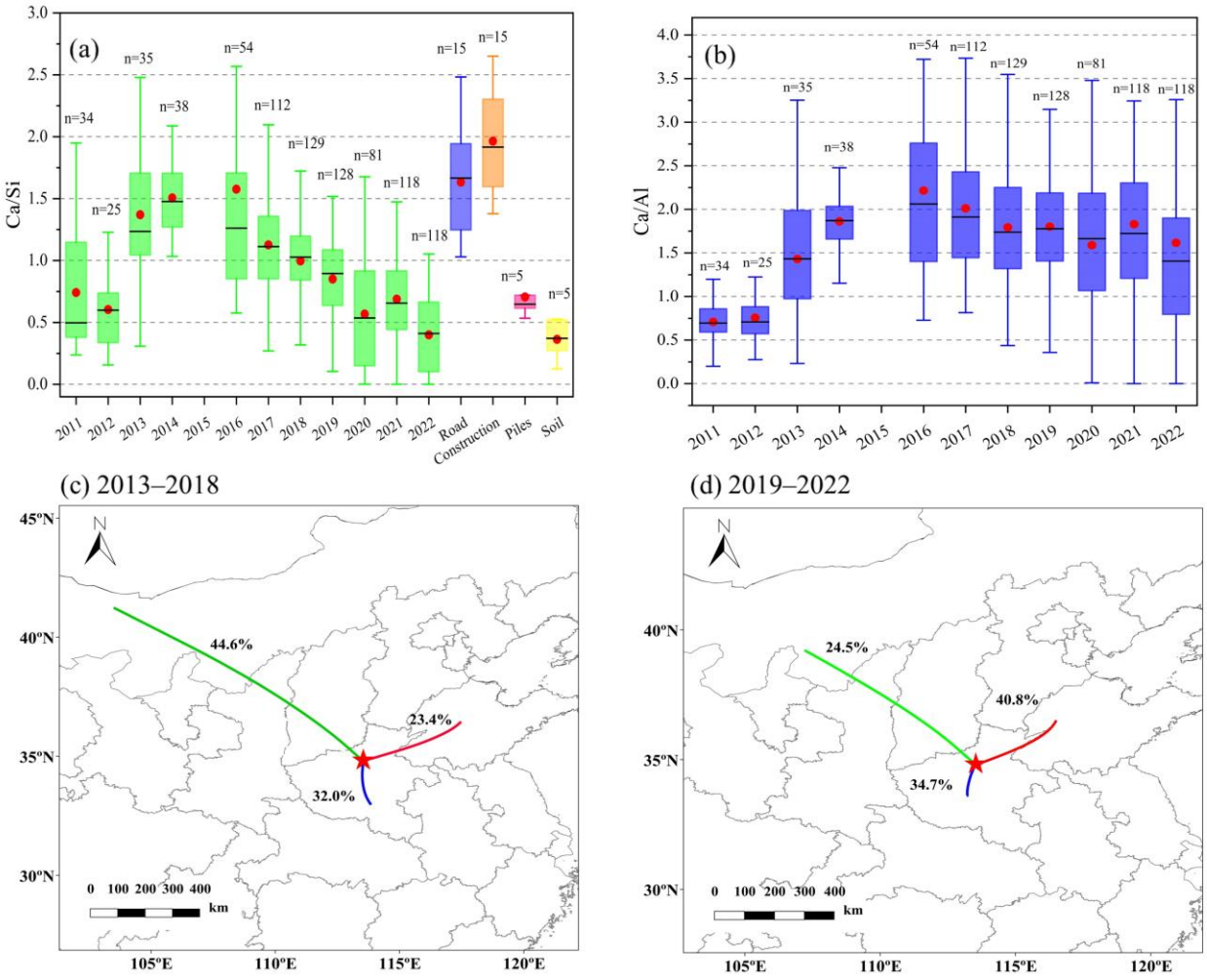

Figure 3. (a) The annual Ca/Si ratios in Zhengzhou from 2011 to 2022 compared with those in various dust sources (specific values and references in Table S5). The red dots and black lines in the box plots represent the annual averages and medians, respectively, with n indicating the sample size. (b) The Ca/Al ratios in Zhengzhou from 2011 to 2022. The red dots and black lines in the box plots represent the annual averages and medians, respectively, with n indicating the sample size. (c) and (d) The transport pathways of CM during 2013–2018 and 2019–2022, respectively.

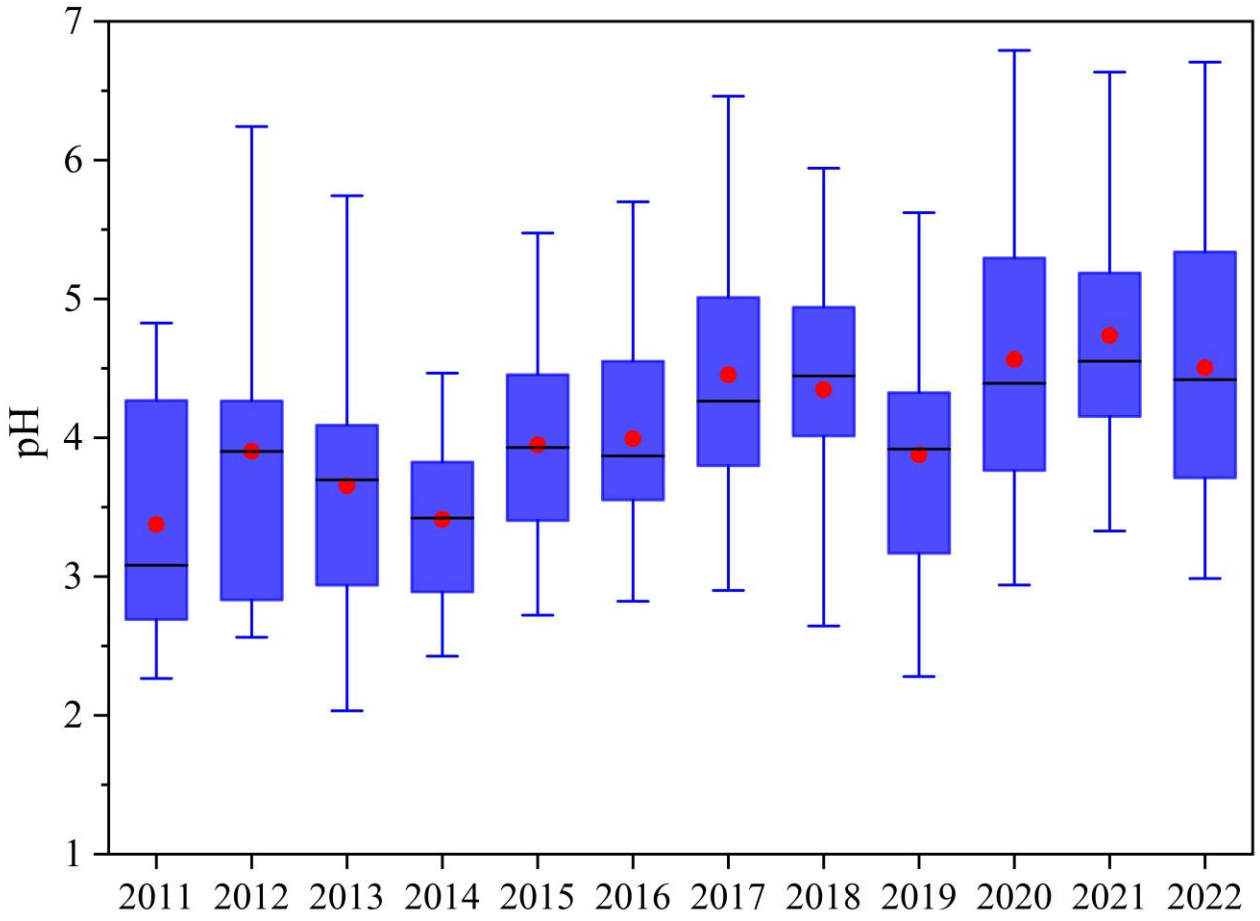

Figure 4. The time series of particle pH in Zhengzhou from 2011 to 2022. In the boxplots, red dots and black lines represent the annual mean and median values, respectively.

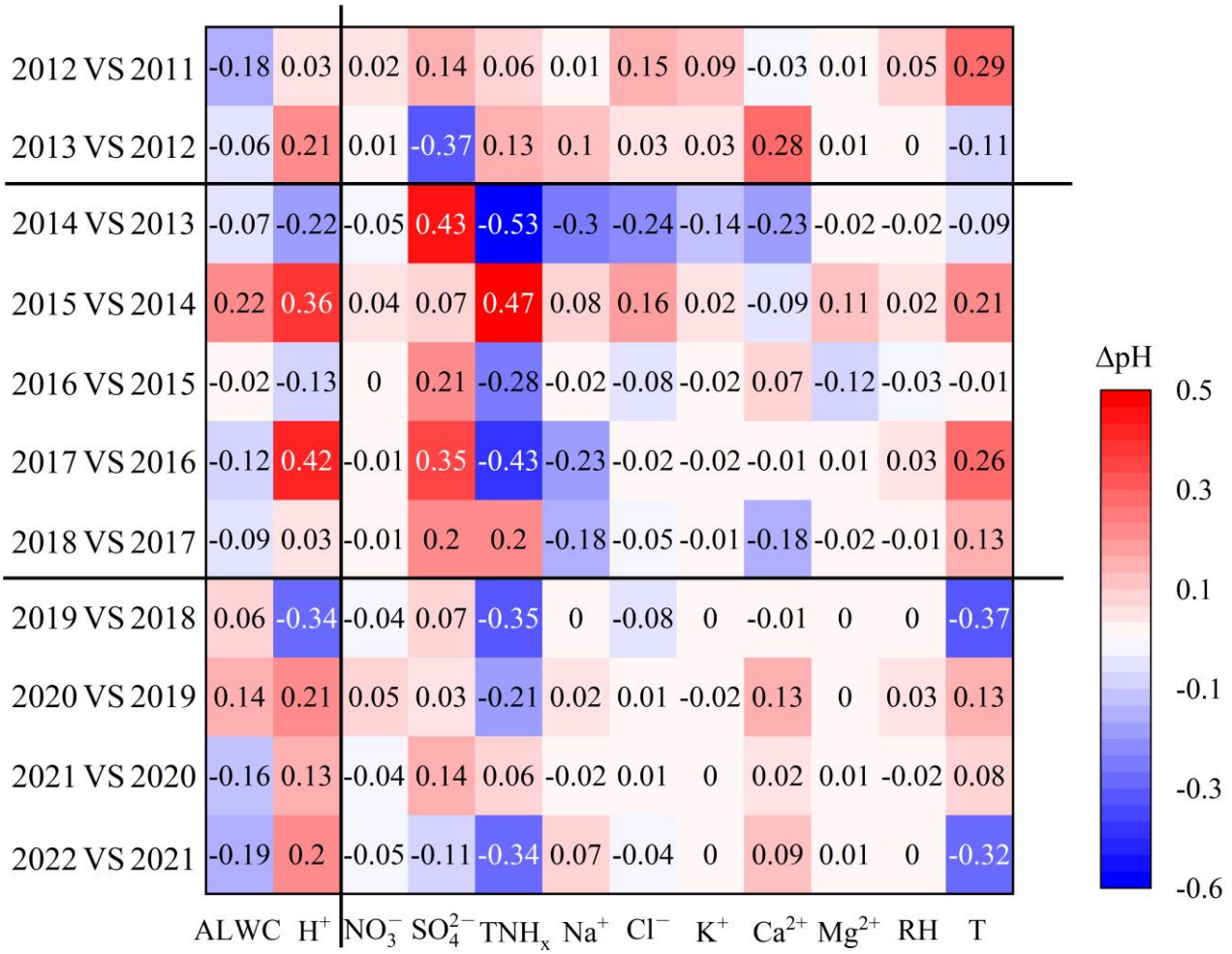

Figure 5. Contribution of each component to the changes in pH (ΔpH) between adjacent years. The difference between component concentrations and meteorological parameters between adjacent years is listed in Table S6.

660 **Table**

661 Table 1. Annual average concentrations of $PM_{2.5}$ and its components from 2011 to 2022 in Zhengzhou,
662 China ($\mu g/m^3$).

Years	$PM_{2.5}$	EC	OC	NO_3^-	SO_4^{2-}	NH_4^+	CM	Ca^{2+}
2011	161.9±81.4	5.1±2.1	13.6±8.6	16.2±11.2	29.6±14.3	13.8±8.3	9.3±7.3	2.0±2.2
2012	157.9±71.2	5.6±2.5	20.0±13.4	20.2±13.7	25.0±11.2	15.0±7.1	8.5±3.4	1.8±0.8
2013	212.4±101.5	6.9±3.8	21.5±10.4	22.7±13.2	38.0±19.9	17.1±6.9	14.6±8.3	3.2±2.1
2014	130.8±48.7	4.6±2.0	14.2±8.2	15.5±10.8	23.4±9.3	10.2±6.2	10.7±4.4	2.1±1.0
2015	146.1±61.0	10.0±4.7	23.2±11.6	20.6±14.5	21.6±9.8	15.7±7.5	12.7±6.8	1.6±0.7
2016	117.4±73.5	4.0±2.8	14.4±10.0	20.4±18.7	17.1±11.3	11.9±10.6	10.8±5.3	2.0±1.1
2017	91.5±61.1	3.1±2.5	13.7±7.5	17.6±15.9	11.8±11.6	8.4±7.9	13.8±6.5	2.0±1.0
2018	76.8±41.6	1.5±0.7	13.4±7.3	16.7±13.5	9.4±6.0	9.7±6.1	8.1±5.7	1.0±0.8
2019	68.4±34.8	1.5±0.8	11.5±6.8	13.8±13.9	8.6±6.4	7.5±6.1	8.5±7.8	0.9±0.9
2020	75.5±31.8	2.1±0.9	13.3±7.9	18.6±14.2	8.3±5.6	6.7±6.6	14.6±7.6	1.6±1.4
2021	71.5±45.9	1.7±0.9	13.0±8.0	15.1±15.1	6.1±4.5	6.8±6.0	8.9±7.0	1.7±1.2
2022	59.5±41.1	1.6±1.5	9.1±8.1	10.0±14.4	7.9±4.5	5.5±5.4	11.2±8.3	2.2±1.1

663